Finite deformation near a crack tip terminated at an interface between two neo-Hookean sheets

Chengyang Mo, Jordan R. Raney, John L. Bassani *

Department of Mechanical Engineering and Applied Mechanics, University of Pennsylvania Philadelphia, PA, 19104, USA

ARTICLE INFO

ABSTRACT

A crack terminating at an arbitrary angle to the interface between two neo-Hookean sheets is investigated under plane stress conditions using finite deformation theory. The asymptotic crack-tip deformation and stress fields are analyzed as a function of the ratio of the moduli and the angle of the crack relative to the interface. Full-field numerical calculations and experimental studies validate the analytical results. A stretch-based crack growth criterion is developed using crack-tip field solutions. Such criterion can predict the delay of crack growth through the bi-material interface observed in experiments and can be extended to any heterogeneity and material.

1. Introduction

The use of heterogeneity is a ubiquitous strategy in nature for producing materials with high toughness. However, challenges arise in engineering applications, for example due to a lack of compatible materials, poor interfacial properties, and practical manufacturing challenges. Two recent examples have used spatial variations in the cross-linker density in studies of failure in heterogeneous polymers, including a soft elastomer (Wang et al., 2019) and a rigid photopolymer (Cox et al., 2019). For the soft elastomer with a crack perpendicular to the interface, heterogeneity introduced by different cross-linking density was found to significantly delay onset of crack growth leading to enhanced toughness (Wang et al., 2019). This effect was shown to be enhanced when the magnitude of the heterogeneity (i.e., the spatial variation in cross-linker ratio) between the two materials increased. However, a mechanistic explanation for the delayed onset of crack growth was not identified. In this paper, this observation is interpreted in terms of the deformation fields around an inclined crack terminating at an angle to the interface between two soft elastomers.

Fracture of soft materials has been studied extensively dating back to the 1950s through experiments and analysis in the setting of finite strain elastostatics. Following the pioneering work of Rivlin and Thomas (1953), the first crack-tip analysis was performed by Wong and Shield (1969). Notably, Knowles and Sternberg considered a class of compressible hyperelastic solids, specifically neo-Hookean solids, with cracks under Mode I conditions (Knowles and Sternberg, 1973, 1974, 1983). They found a smooth crack opening (i.e., with a unique tangent at the crack tip) including for a crack lying on a bi-material interface in which, unlike the case of linear elastic materials, the singular stress field is not oscillatory. A series of papers followed that describe crack-tip fields of generalized neo-Hookean solids under mode I and mixed mode conditions in homogeneous and bi-materials (Geubelle and Knauss, 1994a,b,c). Ru (1997) furthered these studies to include an arbitrary incline angle between two harmonic-type materials.

In this paper, the finite-deformation plane-stress problem of a crack terminating at an arbitrary angle to the interface between two neo-Hookean solids is investigated from both singular crack-tip and full-field finite element analysis and via experiments on 3D

---

printed poly-dimethylsiloxane (PDMS) bi-materials. Such problem has been reasonably developed for linear elastic materials using a small strain analysis, though it has not been fully solved for nonlinear materials under large deformation. The singular field for a crack perpendicular to the interface under Mode I loading was found by Zak and Williams (1963) and for arbitrary bi-material wedge configurations by Bogy (1971), while Cook and Erdogan (1972) and, more recently, Chang and Xu (2007) determined full-field solutions including stress intensity factors for certain Mode I configurations. An arbitrarily oriented crack under anti-plane shear loading that has a special connection to the analysis in this paper was investigated by Bassani and Erdogan (1979).

The crack-tip analysis in this paper builds on the work of Knowles and Sternberg (1973, 1974, 1983) and Geubelle and Knauss (1994a,b,c). Finite element analysis (FEA) as well as experiments are conducted to validate the solutions. A fracture criterion is develop to explain the observed increase in critical applied stretches for initiation of crack growth seen in the work of Wang et al. (2019) and to predict initiation in other bi-material systems.

This paper is organized as follows: Section 2 introduces the general equations that govern the deformation of neo-Hookean hyperelastic solids. Asymptotic solutions are derived in Section 3 for the crack-tip displacements and stresses. Those solutions are shown to be in good agreement with the full-field finite element analysis of Section 4. Experimental evidence of the validity of the analytical solutions is presented in Section 5. The implications of our results as well as an explanation for the delayed initiation of crack growth in heterogeneous systems are discussed in Section 6.

2. Governing equations

Following standard notations, consider a thin sheet of material with material points denoted $\mathbf{x}$ in the undeformed configuration and $\mathbf{y}(\mathbf{x})$ in the deformed configuration. The deformation gradient tensor is $\mathbf{F} = \nabla \mathbf{y}$, and the right Cauchy–Green deformation tensor is $\mathbf{C} = \mathbf{F}^T \mathbf{F}$. Consider an incompressible material, $\det \mathbf{C} = 1$, and the neo-Hookean strain energy density defined as:

$$W = \frac{\mu}{2}(I_1 - 3) \tag{1}$$

where the first invariant of $\mathbf{C}$, $I_1 = \mathrm{tr}\mathbf{C} = \lambda_1^2 + \lambda_2^2 + \lambda_3^2$, λ_i are the principal stretches, and μ is the neo-Hookean material parameter.

The first Piola–Kirchhoff stress $\mathbf{P}$ for this material is:

$$\mathbf{P} = \mu \mathbf{F} - p \mathbf{F}^{-T} \tag{2}$$

where $p = -1/3\mathrm{tr}\sigma$ is the pressure that is undetermined from the constitutive relation, and $\sigma = \mathbf{P}\mathbf{F}^T$ is the Cauchy stress.

The crack problem is considered under plane-stress conditions ($P_{3i} = 0, i = 1, 2$), leading essentially to a 2D problem with symmetry about $x_3 = 0$ (Knowles and Sternberg, 1973) of which the in-plane deformed coordinates y_α, $\alpha = 1, 2$ are sought after. The in-plane components of the first Piola–Kirchhoff stress are:

$$P_{\alpha\beta} = \mu(y_{\alpha,\beta} - \lambda^3 \epsilon_{\alpha u} \epsilon_{\beta v} y_{u,v}) \tag{3}$$

where the out-of-plane stretch $\lambda = F_{33} = (\det F_{\alpha\beta})^{-1}$, $\alpha, \beta = 1, 2$, is derived from the incompressibility condition, and $\epsilon_{\alpha\beta}$ is the two-dimensional alternating symbol ($\epsilon_{11} = \epsilon_{22} = 0, \epsilon_{12} = -\epsilon_{21} = 1$). The nominal traction on a surface with a normal n_β is:

$$t_\alpha = P_{\alpha\beta} n_\beta = \mu(y_{\alpha,\beta} n_\beta - \lambda^{-3} \epsilon_{\alpha u} \epsilon_{\beta v} y_{u,v} n_\beta) \tag{4}$$

The equilibrium condition under plane stress in the absence of body forces, $P_{\alpha\beta,\beta} = 0$, with (3) can be expressed as (Knowles and Sternberg, 1973; Geubelle and Knauss, 1994a; Liu and Moran, 2020a):

$$y_{\alpha,\beta\beta} - \lambda^3 \epsilon_{\alpha u} \epsilon_{\beta v} y_{u,v\beta} - 3\lambda^2 \lambda_{,\beta} \epsilon_{\alpha u} \epsilon_{\beta v} y_{u,v} = 0 \tag{5}$$

3. Asymptotic boundary value problem and solutions

3.1. Boundary value problem

Consider a traction-free crack terminated at an inclined angle ϕ at the interface between two semi-infinite neo-Hookean sheets with crack-tip polar coordinates defined in the undeformed configuration as shown in Fig. 1. Solutions are derived below for the deformation $y_\alpha(r, \theta)$ as $r \to 0$. The moduli of the two sheets are $\mu^{(1)}$ and $\mu^{(2)}$, with the ratio of moduli defined as:

$$s = \mu^{(2)}/\mu^{(1)} \tag{6}$$

The region around the crack tip is divided into three wedged regions with separate solutions for $\mathbf{y}$ in each. Let:

$$\mathbf{y} = \begin{cases} \mathbf{y}^{(1)}, & \phi \le \theta \le \pi \\ \mathbf{y}^{(2)}, & \phi - \pi \le \theta \le \phi \\ \mathbf{y}^{(3)}, & -\pi \le \theta \le \phi - \pi \end{cases} \tag{7}$$

A normalized modulus function $\bar{\mu}(\theta) = \mu(\theta)/\mu^{(2)}$ is also defined in each region :

$$\bar{\mu}(\theta) = \begin{cases} 1/s, & \phi \le \theta \le \pi \\ 1, & \phi - \pi \le \theta \le \phi \\ 1/s, & -\pi \le \theta \le \phi - \pi \end{cases} \tag{8}$$
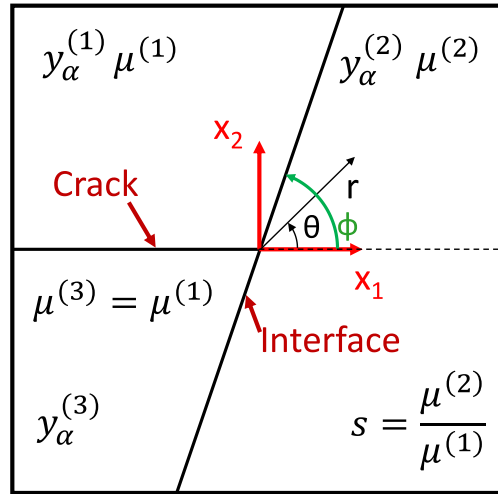
Fig. 1. Schematic of a crack with one tip terminating at an inclined angle ϕ to the interface between two neo-Hookean sheets. r and θ are polar coordinates in the reference configuration. $\phi = 0$ is the interface crack.

Consider the asymptotic form for the out-of-plane stretch $\lambda = O(r^q)$ with $q > 0$, i.e. $\lambda \to 0$ as $r \to 0$ (Knowles and Sternberg, 1973). The governing Eq. (5) and traction (4), neglecting higher order terms in r, become:

$$y_{\alpha,\beta\beta} = 0$$
$$t_\alpha = \mu y_{\alpha,\beta} n_\beta \tag{9}$$

Therefore, in each region

$$\nabla^2 y_\alpha^{(i)} = 0, \quad \text{as} \quad r \to 0 \tag{10}$$

The traction-free boundary condition on the crack surfaces and displacement and traction continuity on the interface, respectively, are:

$$\frac{\partial y_\alpha^{(1)}}{\partial \theta}\Big|_{\theta=\pi} = 0, \quad \frac{\partial y_\alpha^{(3)}}{\partial \theta}\Big|_{\theta=-\pi} = 0 \quad \forall r \tag{11}$$

$$y_\alpha^{(3)}\Big|_{\theta=\phi} = y_\alpha^{(2)}\Big|_{\theta=\phi}, \quad y_\alpha^{(1)}\Big|_{\theta=\phi-\pi} = y_\alpha^{(2)}\Big|_{\theta=\phi-\pi}, \quad \forall r \tag{12}$$

$$\frac{\partial y_\alpha^{(3)}}{\partial \theta}\Big|_{\theta=\phi} = s\frac{\partial y_\alpha^{(2)}}{\partial \theta}\Big|_{\theta=\phi}, \quad \frac{\partial y_\alpha^{(1)}}{\partial \theta}\Big|_{\theta=\phi-\pi} = s\frac{\partial y_\alpha^{(2)}}{\partial \theta}\Big|_{\theta=\phi-\pi}, \quad \forall r \tag{13}$$

3.2. Crack-tip solutions

The traction-free crack and continuity conditions lead to the separable solutions $\mathbf{y}^{(1)}$ and $\mathbf{y}^{(2)}$ in r and θ. The first two leading terms in the series solution for the crack-tip deformation that are separable in the undeformed polar coordinates are (details in Appendix A):

$$y_\alpha = p_\alpha r^m g(\theta) + q_\alpha r\, h(\theta) \tag{14}$$

where $m > 0$, $g(\theta)$ and $h(\theta)$ depend on geometry and material properties while p_α and q_α are amplitude factors that depend on the overall geometry and far-field loading. The angular functions $g(\theta)$ and $h(\theta)$ in each region are (details in Appendix A):

$$g(\theta) = \begin{cases} -\dfrac{s\cos m\phi}{\sin m(\phi - \pi)}\cos m(\theta - \pi), & \phi \leq \theta \leq \pi \\[2mm] \sin m\theta, & \phi - \pi \leq \theta \leq \phi \\[2mm] -\dfrac{s\cos m(\phi - \pi)}{\sin m\phi}\cos m(\theta + \pi), & -\pi \leq \theta \leq \phi - \pi \end{cases} \tag{15}$$

$$h(\theta) = \begin{cases} \left[\dfrac{s}{s\cos^2\phi + \sin^2\phi}\right]\cos\theta, & \phi \leq \theta \leq \pi \\[3mm] \left[\dfrac{(s-1)\sin\phi\cos\phi}{s\cos^2\phi + \sin^2\phi}\sin\theta + \cos\theta\right], & \phi - \pi \leq \theta \leq \phi \\[3mm] \left[\dfrac{s}{s\cos^2\phi + \sin^2\phi}\right]\cos\theta, & -\pi \leq \theta \leq \phi - \pi \end{cases} \tag{16}$$
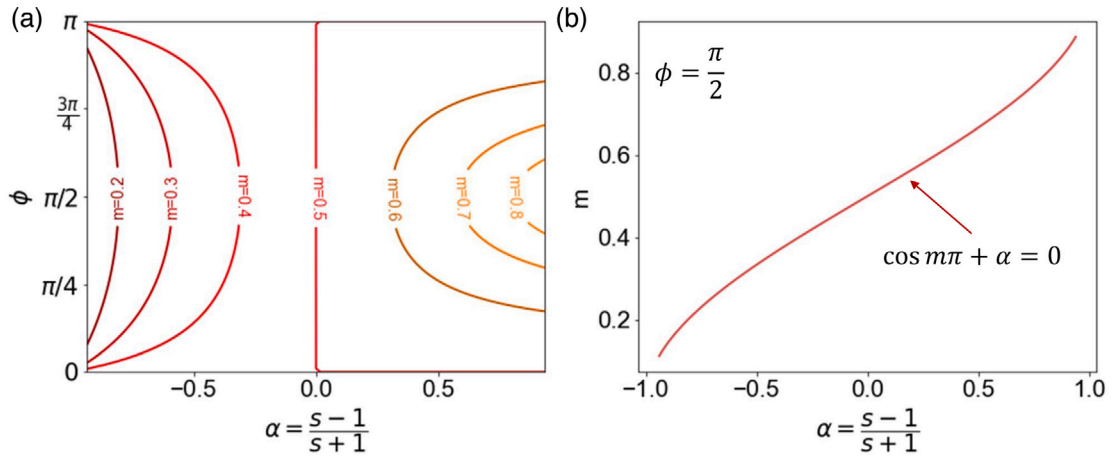
Fig. 2. (a) Exponent m entering (14) from solution to (17) as a function of incline angle ϕ and the heterogeneity factor α as $\alpha = (s-1)/(s+1)$, where $s = \mu^{(2)}/\mu^{(1)}$; (b) m vs. α for a crack perpendicular to the interface ($\phi = \pi/2$).

where m is the smallest positive root of the characteristic equation:

$$\cos m\pi + \alpha \cos m(2\phi - \pi) = 0 \tag{17}$$

with the heterogeneity factor α defined as:

$$\alpha = (s-1)/(s+1) \tag{18}$$

α rescales the ratio of moduli to values between -1 and 1. Eq. (17) is the same characteristic equation derived for the anti-plane shear problem for linear elastic isotropic material (Bassani and Erdogan, 1979), which is not surprising since the two problems share the same governing equations and boundary conditions. There are roots of (17) between 0 and 1 (Bassani and Erdogan, 1979; Ru, 1997) which are plotted in Fig. 2a. In general, m increases monotonically with increasing heterogeneity α. The variation of m with crack orientation is symmetric about $\phi = \pi/2$ and minimized at $\phi = \pi/2$ when $\alpha < 0$ but maximized at $\phi = \pi/2$ when $\alpha > 0$. This trend is similar to results for the plane problems for incompressible linear elastic materials as well (Dundurs' parameter $\beta = 0$) (Bogy, 1971).

For an open crack under large deformation, the following relation should hold (Liu and Moran, 2020a):

$$y_2|_{\theta=\pi} \gg y_2|_{\theta=0} \implies p_2 r^m \gg q_2 r \tag{19}$$

Therefore, since m is generally less than 1, the term involving q_2 can be neglected at large deformation leading to:

$$\begin{aligned} y_1 &= p_1 r^m g(\theta) + q_1 r\ h(\theta) \\ y_2 &= p_2 r^m g(\theta) \end{aligned} \tag{20}$$

The angular functions $g(\theta)$ (15) and $h(\theta)$ (16) are plotted in Fig. 3 for various values of s and ϕ. A few remarks about the solutions follow: Both functions are continuous in θ, which is required by the continuity condition (12). However, the derivatives of the functions are discontinuous at $\theta = \phi$ and $\theta = \phi - \pi$ except in the homogeneous case ($s = 1$). The jump in the derivative has a value of s, which is a result of the traction continuity on the interface (13). Lastly, both functions have zero derivative at the two ends ($\theta = \pm\pi$), which is the result of the traction free condition on the crack surfaces (11).

Before proceeding, a few special cases are worth noting:

- $\phi = 0$: For the interface crack, the solution to the characteristic Eq. (17) leads to $m = \frac{1}{2}$ and the solution is:

$$y_\alpha = p_\alpha r^{1/2} g(\theta) + q_\alpha r \cos\theta \tag{21}$$

  where $g(\theta)$ is defined as:

$$g(\theta) = \begin{cases} s\sin\theta/2, & 0 \le \theta \le \pi \\ \sin\theta/2, & -\pi \le \theta \le 0 \end{cases} \tag{22}$$

  This is the same solution that was obtained by Knowles and Sternberg (1983) that, as in the linear elastic case, leads to a well-defined energy release rate with respect to crack growth.

- $\phi = \pi/2$: This is the case of a crack that is perpendicular to the interface. This solution was not derived in any previous work to the best of our knowledge. The solution is symmetric about the crack plane, $x_2 = 0$, leading to $p_1 = 0$ since y_1 must be an
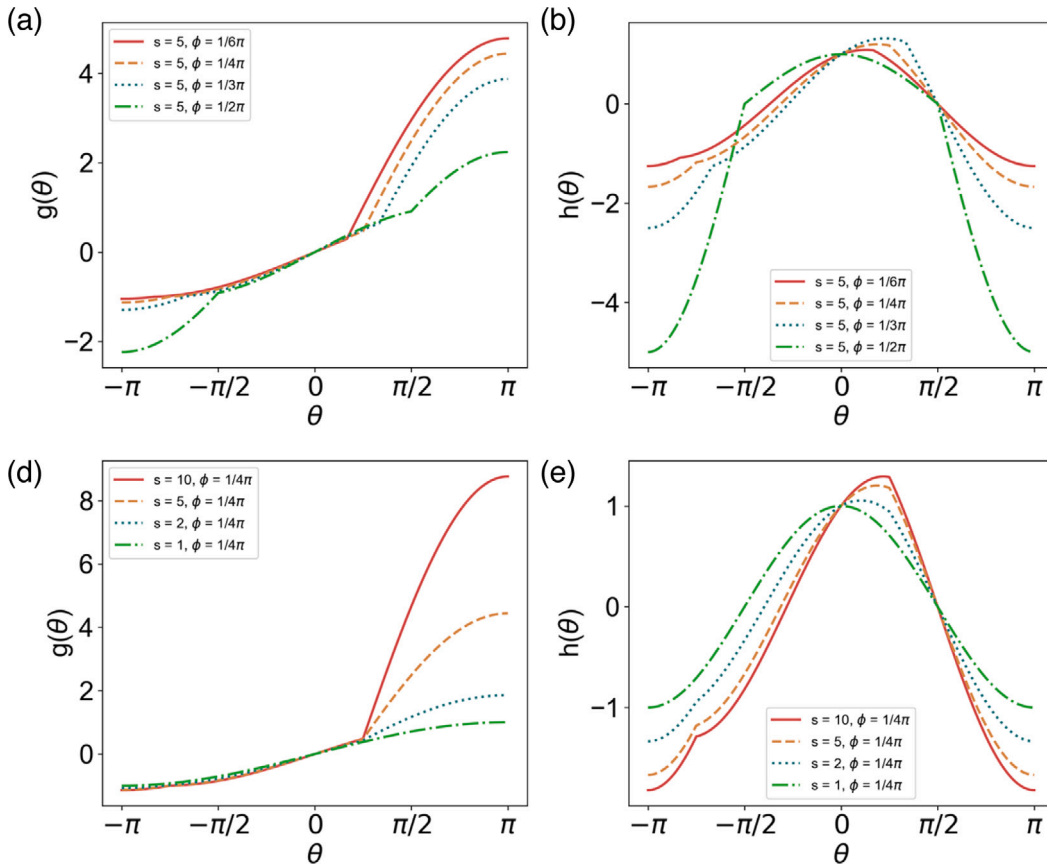
Fig. 3. Solutions of $g(\theta)$ and $h(\theta)$ for various combinations of ratio of moduli s and crack inclination angle ϕ.

even function of θ:

$$
\begin{aligned}
y_1 &= q_1 r \, h(\theta) \\
y_2 &= p_2 r^m g(\theta)
\end{aligned}
\tag{23}
$$

The solution derived (23) suggests a direct relation between the crack-tip opening and displacement in the x_1 direction:

$$
y_2 = \frac{p_2 s^{1/2-m}}{q_1^m} y_1^m
\tag{24}
$$

This relation suggests one can extract the characteristic root m by observing the shape of the deformed crack-tip. The value of m for this configuration is plotted in Fig. 2b as a function of the heterogeneity factor α.

3.3. Stress field around the crack tip

From the solutions in the previous section, the components of the deformation gradient are (see Appendix B):

$$
\begin{aligned}
F_{11} &= p_1 r^{m-1}[mg(\theta)\cos\theta - g'(\theta)\sin\theta] + q_1[h(\theta)\cos\theta - h'(\theta)\sin\theta] \\
F_{12} &= p_1 r^{m-1}[mg(\theta)\sin\theta + g'(\theta)\cos\theta] + q_1[h(\theta)\sin\theta + h'(\theta)\cos\theta] \\
F_{21} &= p_2 r^{m-1}[mg(\theta)\cos\theta - g'(\theta)\sin\theta] \\
F_{22} &= p_2 r^{m-1}[mg(\theta)\sin\theta + g'(\theta)\cos\theta]
\end{aligned}
\tag{25}
$$

The Cauchy stress components are $\sigma_{ij} = F_{jk}P_{ik} = \mu F_{jk}F_{ik}$ (details in Appendix B):

$$
\begin{aligned}
\sigma_{11}/\mu^{(2)} &= \bar{\mu}(\theta)\left[p_1^2 r^{2m-2}G(\theta) + 2p_1 q_1 r^{m-1}GH(\theta) + q_1^2 H(\theta)\right] \\
\sigma_{12}/\mu^{(2)} &= \bar{\mu}(\theta)\left[p_1 p_2 r^{2m-2}G(\theta) + p_2 q_1 r^{m-1}GH(\theta)\right] \\
\sigma_{22}/\mu^{(2)} &= \bar{\mu}(\theta)\left[p_2^2 r^{2m-2}G(\theta)\right]
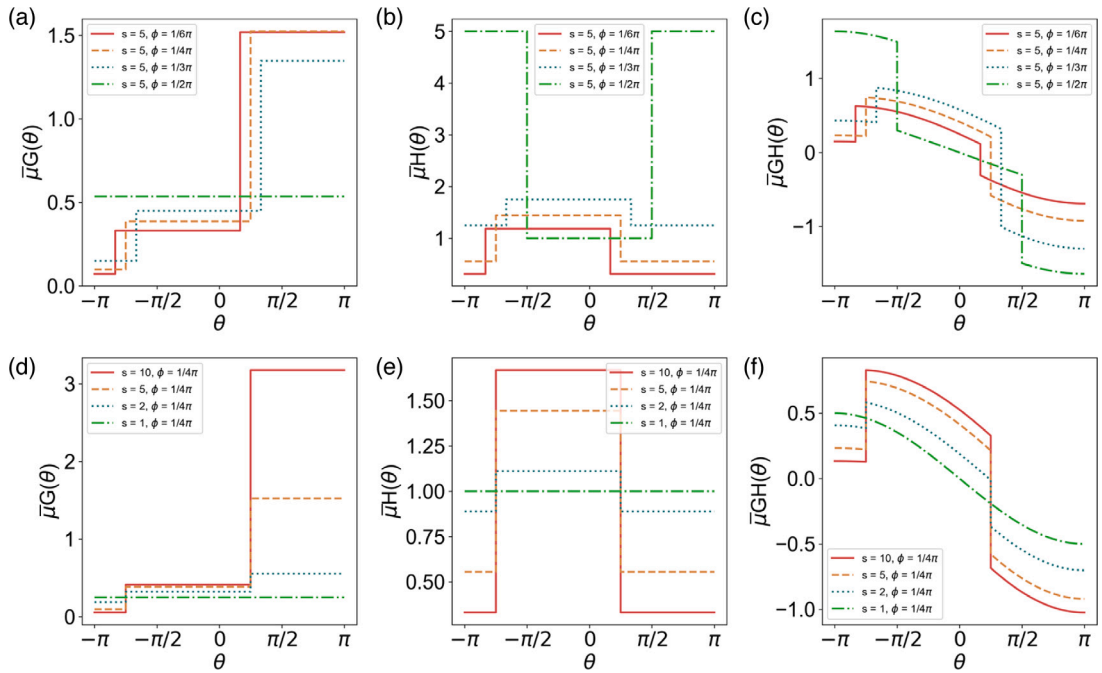\end{aligned}
\tag{26}
$$

Fig. 4. Solutions of $G(\theta)$, $H(\theta)$ and $GH(\theta)$ for various ratio of moduli s and crack inclination angle ϕ.

Define $G(\theta) = m^2 g^2(\theta) + g'^2(\theta)$, $H(\theta) = h^2(\theta) + h'^2(\theta)$ and $GH(\theta) = mg(\theta)h(\theta) + g'(\theta)h'(\theta)$. Utilizing results obtained in (14), these angular functions are:

$$
G(\theta) = m^2 \begin{cases} [\frac{s\cos m\phi}{\sin m(\phi-\pi)}]^2, & \phi \le \theta \le \pi \\ 1, & \phi - \pi \le \theta \le \phi \\ [\frac{s\cos m(\phi-\pi)}{\sin m\phi}]^2, & -\pi \le \theta \le \phi - \pi \end{cases}
\tag{27}
$$

$$
H(\theta) = \begin{cases} [\frac{s}{s\cos^2 \phi + \sin^2 \phi}]^2, & \phi \le \theta \le \pi \\ [\frac{(s-1)\sin\phi\cos\phi}{s\cos^2 \phi + \sin^2 \phi}]^2 + 1, & \phi - \pi \le \theta \le \phi \\ [\frac{s}{s\cos^2 \phi + \sin^2 \phi}]^2, & -\pi \le \theta \le \phi - \pi \end{cases}
\tag{28}
$$

$$
GH(\theta) = m \begin{cases} -\frac{s^2 \cos m\phi}{(s\cos^2 \phi + \sin^2 \phi)\sin m(\phi-\pi)} \cos[(m+1)\theta - m\pi], & \phi \le \theta \le \pi \\ \frac{(s-1)\sin\phi\cos\phi}{s\cos^2 \phi + \sin^2 \phi} \cos(m-1)\theta + \sin(m-1)\theta, & \phi - \pi \le \theta \le \phi \\ -\frac{s^2 \cos m(\phi-\pi)}{(s\cos^2 \phi + \sin^2 \phi)\sin m\phi} \cos[(m+1)\theta + m\pi], & -\pi \le \theta \le \phi - \pi \end{cases}
\tag{29}
$$

One immediate observation from the leading term of (26) is that the Cauchy stress very close to the crack-tip has a $r^{2(m-1)}$ singularity ($0 \le m \le 1$), depending on both the crack inclination and heterogeneity. This result will be discussed below in terms of implications for toughening of the bi-material system. Circumferential variations of Cauchy stress components can be visualized in Fig. 4 by plotting $G(\theta)$, $H(\theta)$ and $GH(\theta)$ normalized by $\bar{\mu}(\theta)$, the ratios of moduli in the different regions. Both $G(\theta)$ and $H(\theta)$ are constant within each region, while $GH(\theta)$ varies within each region. Since σ_{22} only depends on $G(\theta)$, this suggests σ_{22} is constant within each region of the problem. The other two components of Cauchy stress depend on the values of the parameters, with several cases presented in the numerical results section below.

4. Full-field solutions: numerical validation

4.1. Finite element model

To verify the analytical solutions obtained in the above section and to obtain the parameters necessary for full-field solutions, a 2D strip with a single-edge crack (shown in Fig. 5a) is considered under plane stress. A specimen of height H_0 comprises 10 inclined strips of two neo-Hookean solids (1) as is the configuration in experiments in later sections, with parameters $\mu^{(1)}$ and $\mu^{(2)}$, oriented at an angle of ϕ with respect to the horizontal x_1 axis. The horizontal width of each strip is w = $H_0/2$, and the crack of length
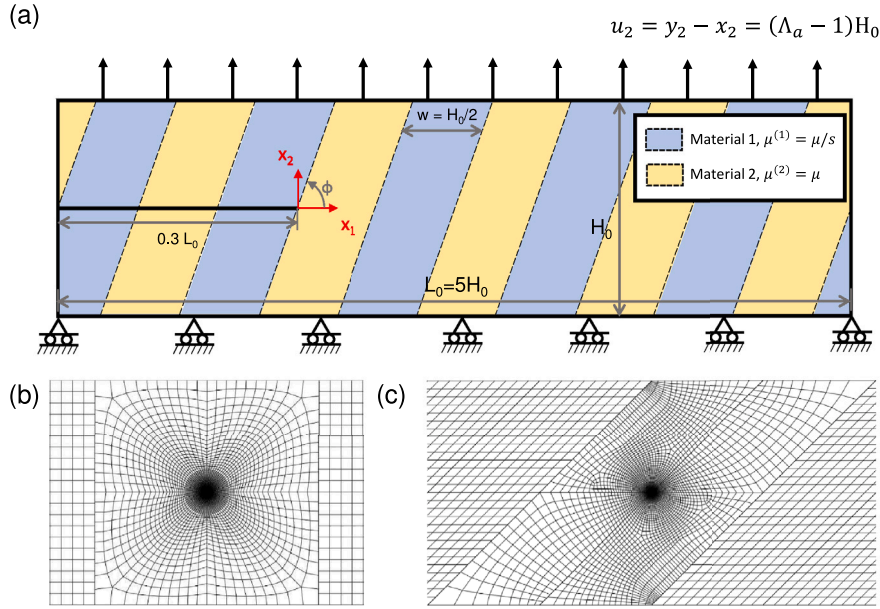
Fig. 5. (a) Specimen setup for finite element analysis. (b) Mesh near crack tip for case of crack perpendicular to the interface; (c) Mesh near crack for case of crack incline at 45° to the interface.

$a = 0.3L_0$ extends from the left edge, where the specimen length $L_0 = 5H_0$. Displacements and tractions are continuous across each bi-material interface. For ratio of moduli $s = \mu^{(2)}/\mu^{(1)} > 1$, the stiffer material (material 2) is directly ahead of the crack-tip, and conversely for $s < 1$. A displacement $u_2 = y_2 - x_2 = (\Lambda_a - 1)H_0$ is applied quasistatically on the top of the specimen, while $u_2 = 0$ on the bottom ($x_2 = -H_0/2$). The shear traction vanishes on the top, the bottom, and the left and right sides of the specimen, and the crack is traction free.

Finite element solutions for large deformations of incompressible, neo-Hookean materials are carried out using ABAQUS. The specimen is meshed with CPS4 quadrilateral elements and radially-focused mesh along r in a small region around the crack-tip ($0 < r < 5 \times 10^{-2}H_0$), with a minimal mesh size of $2.5 \times 10^{-6}H_0$. Outside that circular area, the mesh transitions to a regular grid in two materials near the crack-tip. All other regions are meshed with regular quadrilateral grid. Example meshes for two cases are shown in Figs. 5b and c for reference. Calculations are carried out for various angles of the crack relative to the interfaces as well as different combinations of ratio of moduli.

4.2. Parameter evaluation

To compare the numerical and asymptotic solutions, the three crack-tip parameters p_1, q_1, and p_2 in (20) are extracted from the finite element solutions for the deformed coordinates on a circle with radius $r = r_0 = 5 \times 10^{-4}H_0$ close to the crack-tip. The choice of points is not unique, nor is fitting to displacements rather than stresses, but the following has proven to lead to accurate comparisons. Specifically, the parameters are computed from the deformed coordinates y_1, y_2 at $r = r_0, \theta = 0$ and $r = r_0, \theta = \pi$ from (20) (Liu and Moran, 2020b):

$$q_1 = \frac{y_1(r_0, 0)}{r_0}, \quad p_1 = \frac{y_1(r_0, \pi) - q_1 r_0 h(\pi)}{r_0^m g(\pi)}, \quad p_2 = \frac{y_2(r_0, \pi)}{r_0^m g(\pi)} \tag{30}$$

This guarantees that the fitting from analytical model using evaluated parameters would pass through the coordinates at $r = r_0, \theta = 0$ and $r = r_0, \theta = \pi$ from numerical results.

4.3. Crack perpendicular to the interface, $\phi = \pi/2$

First, the symmetric problem of a crack oriented perpendicular to the interface ($\phi = \pi/2$) is investigated for various ratios of moduli s and various applied stretch Λ_a. The dominance of singularity is first verified by examining the radial variation of the dominant Cauchy stress component σ_{22} directly ahead of the crack-tip ($\theta = 0$) plotted in Figs. 6a and b. For a specimen with ratio of moduli $s = 2$ and various applied stretches Λ_a, the finite element solutions for σ_{22} agree with the predicted singularity near the crack-tip as shown in Fig. 6a. For each simulation, the parameters q_1 and p_2 entering the asymptotic solution (23) are evaluated according to (30) from deformed coordinates at each load step at the same radius $r_0 = 5 \times 10^{-4}H_0$. The finite element results are plotted as points while the comparisons to the solutions (23) are solid lines. From Fig. 6a, it is observed that as applied
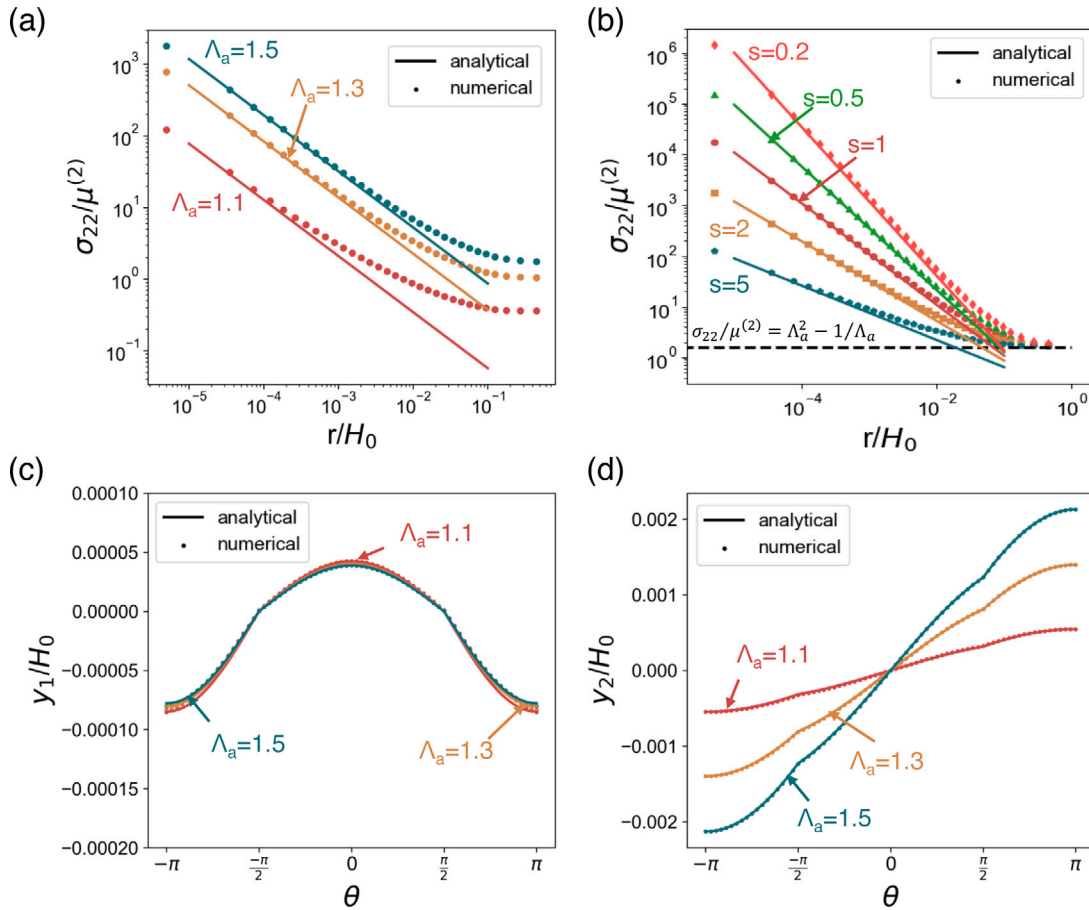
Fig. 6. Cauchy stress σ_{22} vs. distance r ahead of crack tip ($\theta = 0$) for various levels of (a) applied stretch Λ_a for $s = 2$ and (b) ratios of moduli s of $\Lambda_a = 1.5$. Deformed coordinates (c) y_1 and (d) y_2 as a function of θ at $r_0/H_0 = 5 \times 10^{-4}$ at different applied stretch for $s = 2$ for $\phi = \pi/2$.

displacement increases, region of dominance of the asymptotic solutions grows in size, which is expected since large deformation is a key assumption to the asymptotic solutions. The radial variation of the Cauchy stress σ_{22} ahead of the crack-tip is plotted for various ratios of moduli in Fig. 6b at the same applied stretch $\Lambda_a = 1.5$. Again, the stresses follow the predicted singularity from the analytical solutions. A few observations follow from Fig. 6b. First, for all ratios of moduli, the stress converges to a single far field stress: $\sigma_{22} = \mu^{(2)}(\Lambda_a^2 - 1/\Lambda_a)$ which is the uniaxial response of neo-Hookean material. Moreover, the region of dominance of the asymptotic solutions grows in size as the ratio of moduli decreases.

Deformed coordinates are plotted in Fig. 6 along the circular arc with radius $r_0 = 5 \times 10^{-4}H_0$, which is at a distance of about 30 elements away from the crack-tip. For the ratio of moduli $s = \mu^{(2)}/\mu^{(1)} = 2$, Figs. 6c and d are plots of the angular variations of deformed coordinates y_1 and y_2 at various applied stretch. Once again, excellent agreement between the finite element results and asymptotic solutions is clearly seen. Note that the dominant crack-tip displacements are $y_2 - x_2$, which increase monotonically in magnitude as the applied stretch increases, while the displacements $y_1 - x_1$ are much smaller in magnitude and weakly dependent on the applied stretch.

Angular variations of the deformed coordinates y_1 and y_2 for various ratios of moduli $s = \mu^{(2)}/\mu^{(1)}$ are plotted in Figs. 7a and b, respectively, along $r_0 = 5 \times 10^{-4}H_0$. The analytical solutions (23) are in excellent agreement with the finite element results for the major displacements Fig. 7b, while there are differences for the minor displacements seen in Fig. 7a in the region 1 ($\pi/2 < \theta < \pi$) for large heterogeneity, e.g., $s = 5$. The crack-tip opening profiles for various ratios of moduli are also plotted in Fig. 7c, showing that the opening is symmetric under this loading condition for the crack perpendicular to the interface. Moreover, as the ratio of moduli decreases, the crack opening is much larger at the same applied stretch. As the modulus decreases in material 1, larger crack-tip openings are needed to match the same stress level maintained in material 2 (since shear modulus of material 2 is kept constant in all loading cases).

Circumferential variations of the Cauchy stress components are plotted in Fig. 7d–f from the same parameters q_1 and p_2 used for the deformation plots. From (26) and (27), σ_{22} under this configuration is constant with respect to θ at constant r. As a result, σ_{22} extracted from finite element results are normalized by the analytical prediction $\sigma_{22,ana} = \mu^{(2)}p_2^2m^2r_0^{2m-2}$ to visualize all cases in a single plot in Fig. 7d. In this case, with $p_1 = 0$ by symmetry, σ_{11} depends only on $H(\theta)$, while σ_{12} depends on $GH(\theta)$ which is
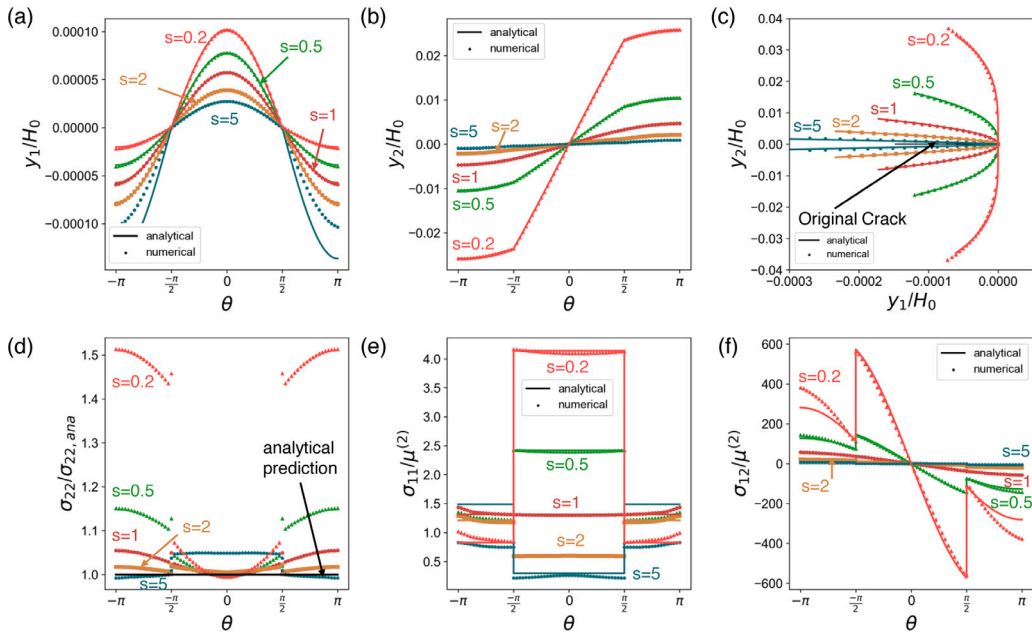
Fig. 7. Comparison of crack-tip asymptotic solutions and finite element results for various ratios of moduli for $\phi = \pi/2$. Circumferential variation of (a) y_1 and (b) y_2, (c) crack-tip openings at different ratios of moduli at applied stretch $\Lambda_a = 1.5$ for $\phi = \pi/2$. (d–f) Circumferential variation of Cauchy stress components $\sigma_{22}/\sigma_{22,\text{ana}}$, $\sigma_{11}/\mu^{(2)}$ and $\sigma_{12}/\mu^{(2)}$ respectively.

evident in the results shown in Fig. 7e and f. Overall, the analytical solutions in Cauchy stresses agree well with the finite element results, but there are deviations particularly in region 1 (See Fig. 1) behind the crack tip. The deviation in both minor displacement and Cauchy stresses in region 1 at larger heterogeneity (small s as $s < 1$ and larger s as $s > 1$) could be possibly explained in two ways: (i) for larger heterogeneity, the region of dominance of asymptotic solutions becomes smaller, as observed in Fig. 6b, moving it outside the region of dominance; (ii) The radial focused mesh includes elements with a larger aspect ratio that can affect the numerical accuracy, especially under large deformation near the crack tip.

4.4. Results for $\phi = \pi/4$

The asymmetric problem with an inclined interface is investigated next for a crack terminating at an angle $\phi = \pi/4$ to the interface. Finite element results for various ratios of moduli s are presented, and again for each simulation, the parameters p_1, q_1 and p_2 are evaluated according to (30), extracted from deformed coordinates from finite element results. The Cauchy stress σ_{22} ahead of the crack tip is plotted in Fig. 8a for varying applied stretch Λ_a and $s = 2$ and in Fig. 8b for various ratios of moduli and $\Lambda_a = 1.5$. Once again, good agreement is found between finite element results and analytical solutions for the crack-tip singular field. Note, for the inclined crack, the Cauchy stress σ_{22} directly ahead of the crack no longer converges to the same nominal stress for various ratios of moduli at the same applied stretch due to the asymmetry in the problem. The deformed coordinates along a circle of radius $r_0 = 5 \times 10^{-4} H_0$ extracted from each simulation are plotted in Figs. 8c and d. Excellent agreement for y_2 is found except for small deviations for y_1 observed in region 3 (see Fig. 1).

For the inclined crack, finite element results for $s > 1$ and $s < 1$ are plotted separately in Figs. 9 and 10, respectively, since the magnitude of the deformations vary significantly. The deformed coordinates y_1 and y_2 for the case in which stiff material is placed directly ahead of the crack tip ($s > 1$) are plotted as points in Figs. 9a and b for various ratios of moduli. The finite element results again are in good agreements with the analytical solutions including the stress components as shown in Figs. 9d–f.

The finite element results for the case in which the soft material is directly ahead of the crack tip ($s < 1$) are shown in Fig. 10. It can be immediately observed that the crack-tip opening is one order magnitude larger than that for the case of $s > 1$ as shown in Fig. 10a and b. As a result, the crack-tip opening is much larger compared to the initial crack as shown in Fig. 10c. This also leads to orders of magnitude larger Cauchy stresses as shown in Fig. 10d–f. Nevertheless, the analytical solutions still are in good agreement with the finite element results overall.

5. Experimental validation

5.1. Experimental methods

Long thin strips of PDMS specimens were 3D printed using direct ink writing (DIW). A custom-built multi-material DIW printer was used to print specimens with the geometry described in Fig. 5, with $H_0 = 20$ mm and a thickness of 0.6 mm. The mechanical
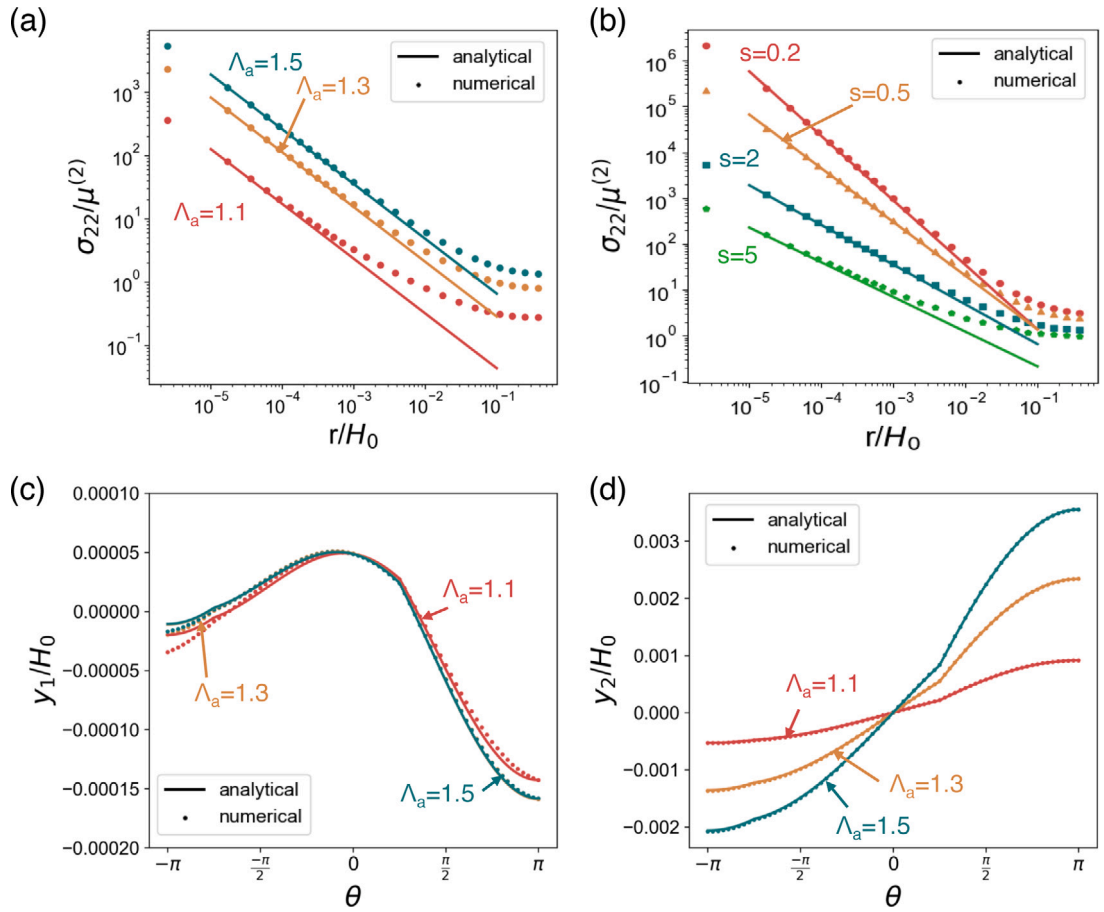
Fig. 8. Cauchy stress σ_{22} vs. distance r ahead of crack tip ($\theta = 0$) for various levels of (a) applied stretch Λ_a at $s = 2$ and (b) ratios of moduli s at $\Lambda_a = 1.5$. Deformed coordinates (a) y_1 and (b) y_2 as a function of θ at $r_0/H_0 = 5 \times 10^{-4}$ at different applied stretch for $s = 2$ for $\phi = \pi/4$.

Table 1
Configurations for all specimens experimentally tested.

	s	α	φ
Specimen 1	1	0	$\pi/2$
Specimen 2	2.4	0.41	$\pi/2$
Specimen 3	16	0.88	$\pi/2$
Specimen 4	2.4	0.41	$\pi/3$
Specimen 5	2.4	0.41	$\pi/4$

behavior of PDMS is well described by a neo-Hookean hyperelastic model (Kim et al., 2011). The PDMS precursor ink used for printing consists of 15% SE-1700 (Dow Corning) and 85% Sylgard 184 (Dow Corning) in mass with various amount of polymer base to cross-linker ratio to obtain different moduli (Shan et al., 2015). PDMS with less cross-linker results in a material with a lower stiffness. In this work, the material in region 2 is kept constant, i.e., region 2 is a stiff PDMS (using cross-linker ratio of 10:1) while material in region 1 is a softer PDMS (cross-linker ratio of 20:1 and 30:1). Specimens were subsequently cured at 100 °C for 1 h after printing. The elastic moduli were obtained from uniaxial tensile tests of PDMS specimens with different cross-linker ratios, as shown in Fig. 11a, with the ratio between elastic modulus with respect to 10:1 crosslinked PDMS also reported in Fig. 11b.

To investigate the effect of material heterogeneity, three specimens were fabricated with the crack oriented perpendicular to the interface ($\phi = \pi/2$) with various heterogeneity. Specimen 1 was a homogeneous specimen, with both regions printed with the same 10:1 base:cross-linker ratio. The soft region in the other two specimens were printed with 20:1 and 30:1 base:cross-linker ratios, leading to ratios of moduli of $s = 2.4$ and $s = 16$, respectively. Additionally, two specimens with the same ratios of moduli $s = 2.4$ were fabricated with a crack inclined interface ($\phi = \pi/3, \pi/4$) to investigate asymmetry. All five specimen configurations are summarized in Table 1. Specimen 1 was homogeneous, and the other four were bi-material specimens.

Specimens 2 and 3 with the crack perpendicular interface ($\phi = \pi/2$) were pre-cut with a razor blade such that the cracks were a few millimeters behind the interface. Prior to testing, the specimens were preloaded in tension until the crack grew to the desired
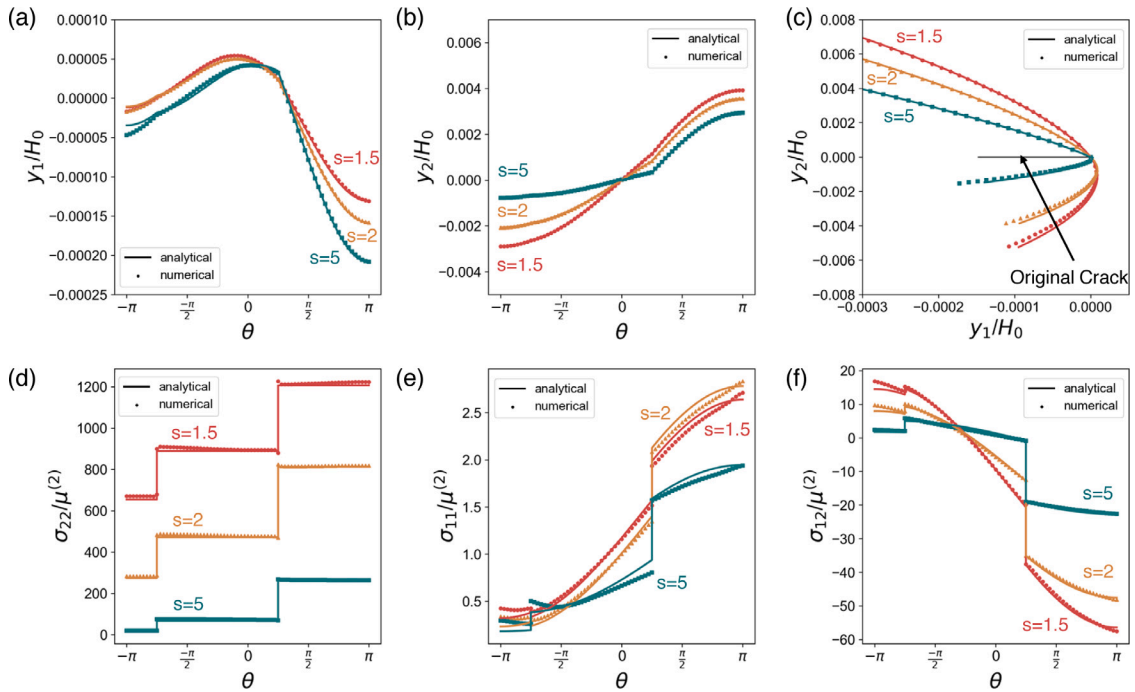
Fig. 9. Comparison of crack-tip solutions and finite element results for various ratios of moduli ($s > 1$) for $\phi = \pi/4$. Circumferential variation of (a) y_1 and (b) y_2; (c) crack-tip openings at different ratios of moduli at applied stretch $\Lambda_a = 1.5$. (d–e) Circumferential variation of Cauchy stress components σ_{22}, σ_{11} and σ_{12}, respectively.
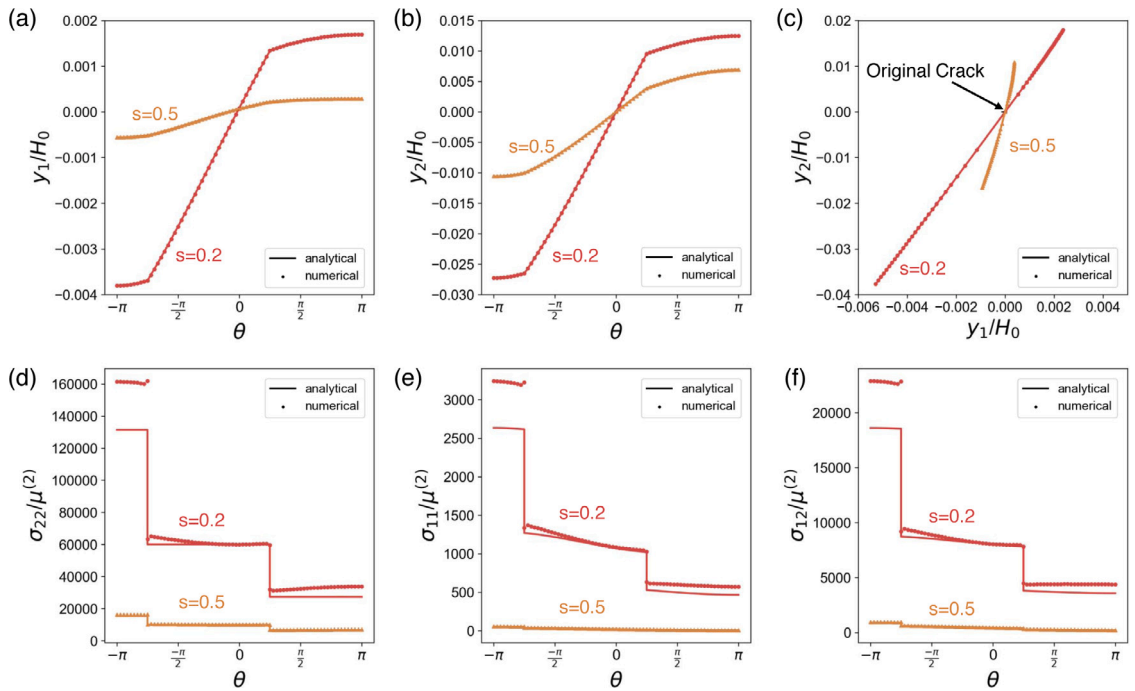

Fig. 10. Comparison of crack-tip solution and finite element results for various ratios of moduli ($s < 1$) for $\phi = \pi/4$. Circumferential variation of (a) y_1 and (b) y_2; (c) crack-tip openings at different ratios of moduli at applied stretch $\Lambda_a = 1.5$. (d–f) Circumferential variation of Cauchy stress components σ_{22}, σ_{11} and σ_{12}, respectively.
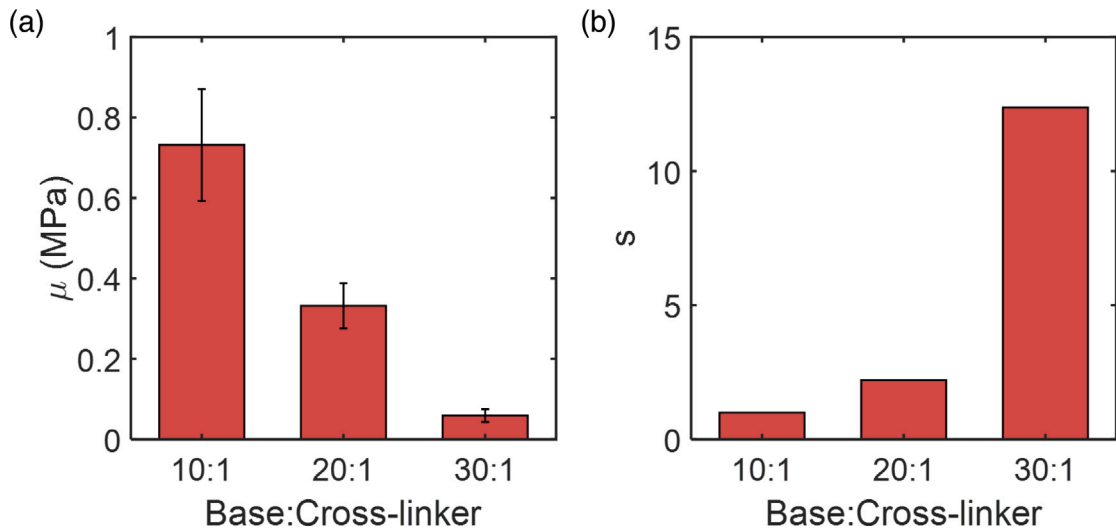
Fig. 11. (a) Shear modulus of PDMS with different cross-linker ratios. (b) Resulting ratios of moduli with respect to 10:1 base to cross-linker ratio PDMS corresponding to specimens in Table 1.

length to ensure the razor blade cut did not affect the crack-tip opening shape. For the heterogeneous specimens, the preload was increased until the crack just reached the interface. For the homogeneous specimen (specimen 1), the preload was removed after the crack grew an additional 5 mm. After preload, the specimen was unloaded to an unstressed configuration and then loaded again up to failure. For specimens with inclined interfaces (specimen 4 and 5), cracks were pre-cut as close to the interface as possible before loading until failure. During the loading process the deformation of the crack tip was recorded using a 4 K camera with a resolution of 10.5 μm/pixel. In addition, speckle patterns were applied on the surface of the specimen using an airbrush for Digital Image Correlation (DIC). DIC analysis for specimens was conducted using MATLAB Ncorr 2D package with subset size of 20 pixels and subset spacing of 5 pixels.

5.2. Experimental results

First, for a crack perpendicular to the interface ($\phi = \pi/2$), the shape of the crack tip should follow the power law relation (24), where the power m is a function of the material heterogeneity. Crack tips of the three specimens (specimen 1–3) with different ratios of moduli across the interface (as indicated in Table 1) are shown in Figs. 12a–c. From here on, the heterogeneity factor α(18) is used interchangeably with ratio of moduli s to compare with analytical solutions. The crack tip of specimen 1 (homogeneous specimen) is smooth and resembles a parabola. As the ratios of moduli increases, the crack tip sharpens. The crack-tip openings were analyzed quantitatively by extracting the crack-tip coordinates (red scatters in figure) from the images. Then the extracted coordinates were fit to the power law relation. The fitted crack-tip for each case is also displayed as a cyan line. The experimentally extracted crack-tip opening exponent agrees very well with the analytical solution of the characteristic Eq. (17), as shown in Fig. 12d.

In addition to the crack-tip opening, the full-field displacements were also characterized using DIC. DIC results of homogeneous specimen 1 and also specimen 3 with its large heterogeneity difference were analyzed. After obtaining full-field displacements, the deformation gradient around the crack tip was computed by local spatial derivatives. The values of F_{21} and F_{22} straight ahead of the crack tip ($\theta = 0$) are plotted in Figs. 13a and b. The component F_{21} straight ahead of the crack tip is close to zero as shown in Fig. 13a, which agrees with the analytical solutions. The component F_{22} close to the crack tip exhibits singular behavior as shown in Fig. 13b. From log–log plots of F_{22}, the singularity for the homogeneous specimen is −0.45 while for the heterogeneous specimen it is -0.21. Analytical solutions in (25) indicate that the singularity of F_{22} equates to $m-1$ leading m being 0.55 and 0.79 respectively. The values of m extracted from the DIC results were also plotted in Fig. 12d, further validating the analytical solutions. The circumferential variation of component F_{21} and F_{22} for both specimens at $r = 0.5$ mm were plotted in Fig. 13c and d. The DIC result agrees well with the analytical solutions, which are plotted as dashed lines. Additional accuracy in the result can be obtained if higher resolution imagery can be employed to capture crack-tip deformation.

Secondly, three specimens with same ratios of moduli ($s = 2.4$) but different inclination angles were also experimentally tested: images before and after crack growth are shown in Fig. 14. Cracks in both specimens with an inclined crack angle were deflected along the interface in the softer region and never reached the interface. After deflection, the crack continued to grow along the interface until it reached the grip section. In contrast, the crack always propagated through the interface when it was originally perpendicular to the interface.
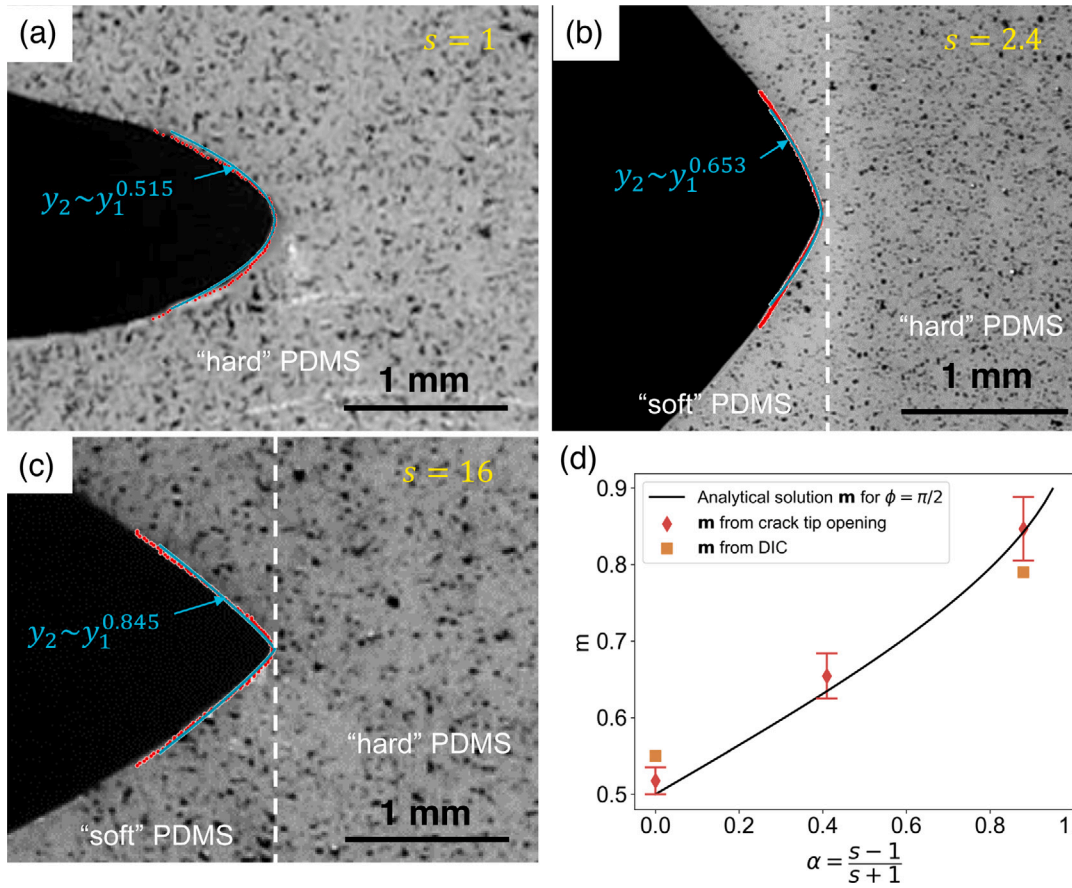
Fig. 12. (a)–(c) Crack-tip opening for specimens with cracks perpendicular to the interface and ratios of moduli $s = 1$, $s = 2.4$ and $s = 16$ respectively. Crack-tip openings are traced using image analysis as red scatters in the plot. The best fit $y_2 \sim y_1^m$ is shown in each plot with corresponding m. (d) extracted crack-tip shape exponent m vs. α with $\phi = \pi/2$ with crack-tip opening (Error bars: variation of m with choice of crack-tip location and number of points for fitting) and DIC.

6. Crack growth criterion

The experiments show that when the crack is perpendicular to the interface, if the material ahead of the crack is held fixed then the critical applied stretch at the initiation of crack growth increases with the stiffness of the material behind the crack tip (Fig. 15a). This toughening induced from the heterogeneity was also observed in the experiments of Wang et al. (2019). In addition, the crack opening profiles depend on the heterogeneity as seen in Fig. 12. The observed critical applied stretches in this work are very similar to those of Wang et al. (2019) despite the fact that the specimens in this work are 3D printed rather than cast, and have much larger region widths and, therefore, fewer periods. From the analytical solutions (Section 3) and finite element analysis (Section 4), a crack growth criterion is developed to predict the increasing delay in crack growth associated with an increased degree of heterogeneity across the interface, thereby explaining the apparent toughening observed in experiments.

The criterion for initiation of crack growth is intended to resolve: (i) the direction of crack growth initiation and (ii) the load required for initiation of crack growth. In considering fracture of soft materials, two criteria have been considered (Long and Hui, 2015). One that is well posed for homogeneous materials is a fracture criterion based on the energy release rate (Thomas, 1958). For the crack tip terminated at the interface, the energy release rate is not well defined, for example path-independent integrals are not defined for the bi-material samples. Hence, the energy release rate criterion is not well suited for this problem.

Another fracture criterion is based upon local quantities defined in the neighborhood of the crack tip. Failure in elastomers and polymers is often described by breaking of polymer chains, which is directly related to the local stretch around the crack tip (Thomas, 1958). Consequently, a stretch based criterion can be used to investigate crack growth in polymer. This approach has been previously employed to predict the direction of crack growth for a center cracked specimen of rubber with mixed mode loading (Hamdi et al., 2007), resulting in the direction of crack growth always being perpendicular to the loading direction regardless of the crack inclination relative to loading direction. Consider a criterion for crack growth in the direction perpendicular to the direction of the maximum principal stretch when it reaches a critical value of that stretch at a distance r_c ahead of the crack-tip.
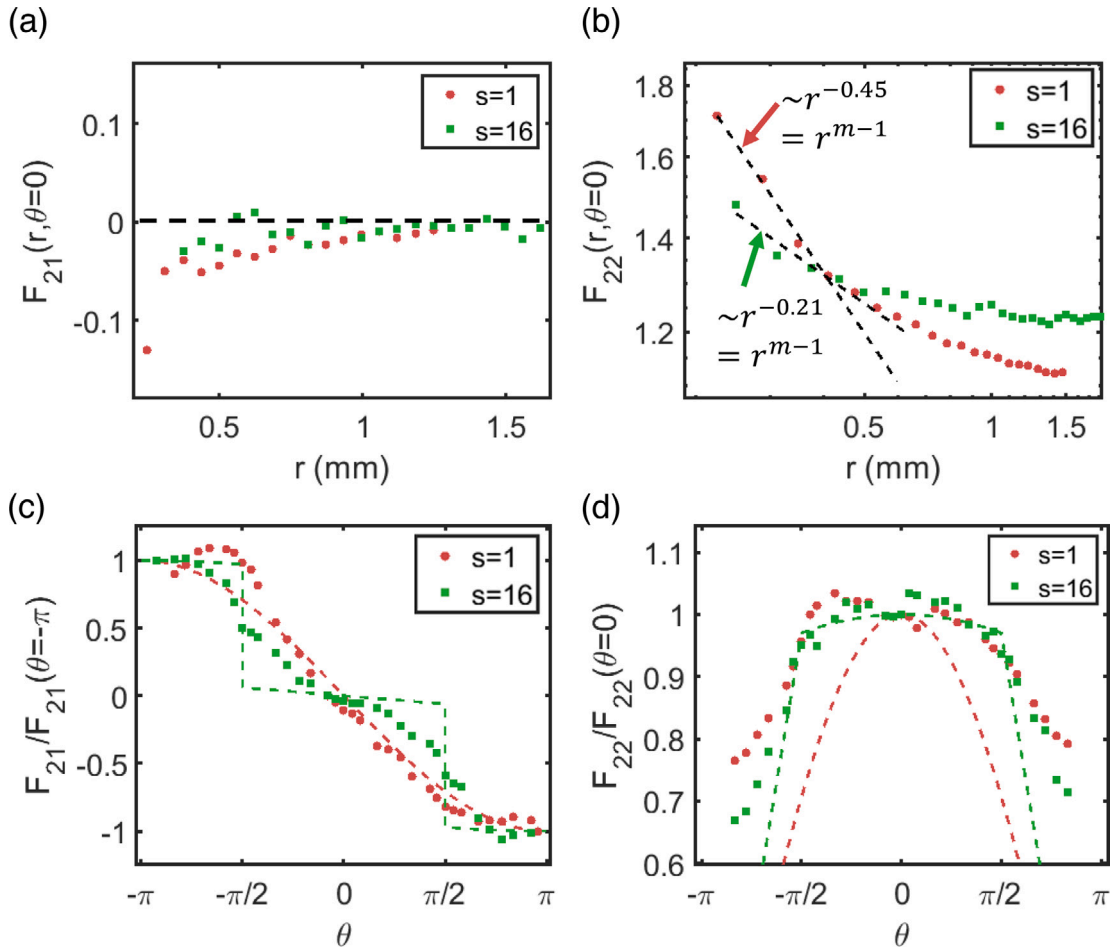
Fig. 13. Deformation gradient calculated from DIC for the homogeneous specimen (specimen 1) and the heterogeneous specimen (specimen 3) at $\Lambda_a = 1.25$: (a–b) F_{21} and F_{22} vs. r ahead of the crack tip ($\theta = 0$); (c–d) F_{21} and F_{22} vs. θ for $r = 0.5$ mm.

That distance is associated with a characteristic microstructure length scale that should fall within the region of dominance of the asymptotic crack-tip field of Section 3. Specifically, the criterion can be written as:

$$\lambda_1(r_c) = \lambda_c \tag{31}$$

where λ_1 is the maximum principal stretch and λ_c is the critical stretch associated with the material. A critical stretch criterion has been widely adopted for ductile fracture of metals. Recently, this criterion was experimentally validated in elastomers by tracking the principal stretch direction as crack propagates under mixed-mode fracture (Lu et al., 2021).

For the analytical solution, the principal stretches are computed by finding eigenvalues of the left Cauchy–Green tensors, computed in full in Appendix B. When considering initiation of crack growth, only the leading term with a singularity of r^{2m-2} is considered:

$$\mathbf{B} = r^{2m-2}G(\theta) \begin{bmatrix} p_1^2 & p_1 p_2 \\ p_1 p_2 & p_2^2 \end{bmatrix} \tag{32}$$

where $G(\theta)$ is defined in (27). The maximum principal stretch and principal direction can be computed by finding the eigenvalues and eigenvectors of the left Cauchy green tensors:

$$\lambda_1^2 = (p_1^2 + p_2^2)r^{2m-2}G(\theta) \tag{33a}$$

$$\mathbf{n}_1 = [p_1 \quad p_2]^T \tag{33b}$$

One interesting observation from ((33)b) is that the principal direction does not have circumferential dependence. Hence, no matter where the maximum principal stretch is achieved, the crack will always propagate in one direction given by p_1 and p_2 in ((33)b). Moreover, near the crack tip, the following relation should hold true for large deformation: $y_2 \gg y_1$. Both solutions have terms with
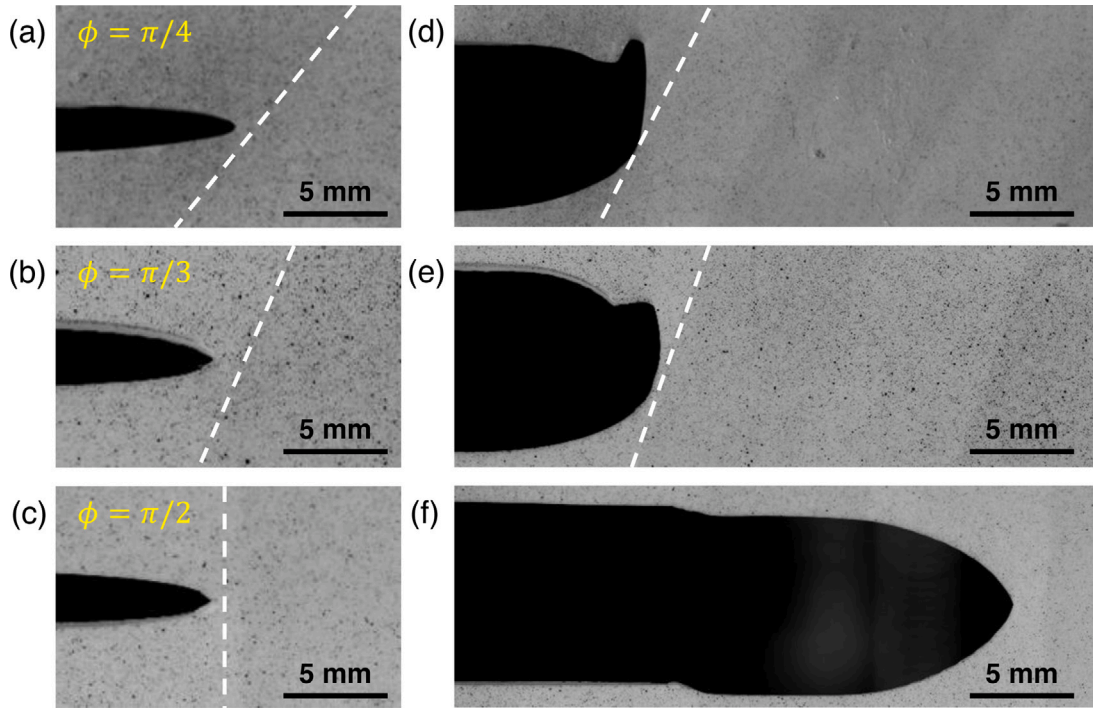
Fig. 14. Crack-tip openings for specimens with inclined interfaces, each with the same ratio of moduli ($s = 2.4$): before crack growth (a) $\phi = \pi/4$, (b) $\phi = \pi/3$, (c) $\phi = \pi/2$; after crack growth (d) $\phi = \pi/4$, (e) $\phi = \pi/3$, (f) $\phi = \pi/2$ (Full video included in supplementary information).
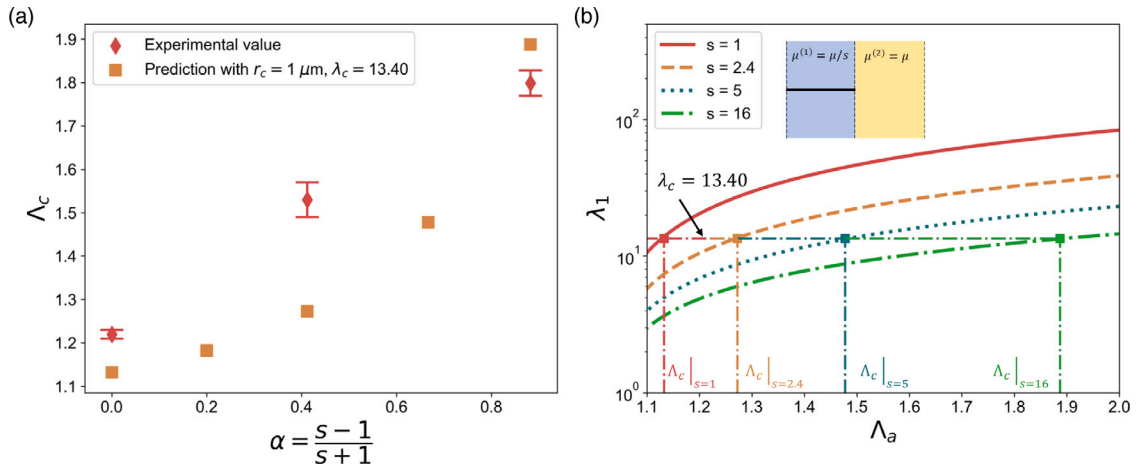

Fig. 15. (a) Experimental observations of critical applied stretch for initiation of crack growth (Error bars: S.D., n = 3); (b) Numerical results of principal stretch at $r_c = 1$ μm ahead of the crack tip vs. far field applied stretch Λ_a at various heterogeneity. The critical applied stretch Λ_c can be predicted, here plotted as squares in panel (a).

the same singularity, implying that $p_2 \gg p_1$. Hence the principal direction is essentially the x_2 direction, meaning the crack should always propagate straight ahead ($\theta = 0$). The maximum principal stretch is:

$$\lambda_1 = p_2 m \cot \frac{m\pi}{2} r^{m-1} = \lambda_c \tag{34}$$

Fracture propagates through the interface at applied stretch Λ_c when the principal stretch reaches a critical level λ_c a distance r_c ahead of the crack tip. The corresponding amplitude p_2 can be obtained from the finite element analysis given (30).

In both the experiments and the finite element analysis, the material ahead of the crack tip is kept constant. The characteristic length r_c is related to the characteristic dimension of the microstructure of PDMS. In an ideal polymer network, after a polymer chain is fractured, load concentrates onto the next chain. Hence, the characteristic length for the fracture criterion can be estimated

from the end to end stretched chain length between the crosslinker. For PDMS with 10:1 crosslinking ratio which is the material kept constant ahead of the crack tip, the backbone of the linear chain contains $N = 700$ chemical units (Cai et al., 2015). With the length of each monomer $b = 1.3$ nm (Cai et al., 2015), this leads to $r_c = Nb \approx 1$ μm. This choice of r_c is an upper bound, as the chains are not fully stretched, while this falls within the region of dominance. Hence a smaller value, given the separable form of the crack tip fields, would essentially lead to the same prediction with an appropriate λ_c in (31)–(34).

Using this characteristic length parameter, the principal stretches for various heterogeneity considered in the experiments vs. applied stretch are estimated in Fig. 15b. Since the material ahead of the crack is held fixed, a constant λ_c is used to determine the critical applied stretch for crack growth. From the measured applied critical stretch Λ_c from experiments, the λ_c that minimizes the square error between all three experiments and predictions is found to be $\lambda_c = 13.4$. This value of λ_c at r_c provides good predictions across all heterogeneities. In a uniaxial tensile test, the PDMS used in this work ruptured at approximately a stretch of 5, which is on the same order of magnitude of the λ_c used in the criterion. The criterion is capable of providing quantitative prediction for the initiation of crack growth through the bi-material interface. In particular, the critical applied stretch for any heterogeneity can be computed using this fracture criterion from the finite element analysis, for example as given in Fig. 15a for $\alpha = 0.2$ and $\alpha = 0.7$. The predicted results also agree well with the observation in previous work (Wang et al., 2019). Furthermore, from singularity analysis, which is supported by finite element results (e.g., Fig. 6b), the stress stretch state ahead of the crack tip is much higher if the material ahead of the crack (in Section 2) is softer ($s < 1$). This suggests that the crack would not be deterred by the interface. Indeed, this criterion can be applied to other polymeric systems as well to predict the fracture behavior through bi-material interfaces from estimates of the characteristic length scale r_c, the critical stretch λ_c, and the ratios of moduli s.

Lastly, we note that the prediction that the crack will always propagate straight ahead of the crack are not in accord with experiments with specimens with interfaces inclined relative to the crack. We recognize the difference between the ideal configuration of the mathematical problem and the experiment. The ideal case is simplified as the interface is assumed to be perfectly sharp and the crack tip to be exactly at the interface. However in reality, we do not expect the interface between two regions to be sharp, both due to printing errors and to possible diffusion of cross-linker during the thermal curing process. Additionally, the crack is pre-cut using a razor blade which leads to difficulty in achieving a crack that exactly terminates at the interface. He and Hutchinson (He and Hutchinson, 1989) discussed the ramification of cracks approaching the interface at an inclined angle, where they argued the crack would curve away from the interface if the material ahead of the interface is stiffer ($\alpha > 0$) which is what was observed in the experiments. The location of the initial crack tip could have a significant effect on the direction of crack growth. Due to the nonlinearity of our material, we cannot confidently reach the same conclusion without further studies.

7. Conclusions

Crack-tip solutions for a crack terminated at an inclined angle at an interface between two neo-Hookean sheets have been developed using asymptotic analysis with finite deformation elastostatics. The components of displacement, stretch, and Cauchy stress have been derived from the solutions near the crack tip. The crack-tip fields exhibit varying singularity as the incline angle and heterogeneity vary, as in the linear elastic case. As the stiffness of the material ahead of the crack increases (larger α or s) the power of singularity decreases.

The analytical solutions are validated by finite element analysis showing excellent agreement in both deformed coordinates and Cauchy stress components for various heterogeneities and incline angles. Some discrepancies are observed, which could be attributed to the extremely large distortions of the meshes.

Experiments also validate the analytical solutions by matching crack-tip exponents in the singular solution with extracted crack-tip opening. Additionally, the local deformation gradient extracted using DIC also agrees with the analytical solutions.

Lastly, using a stretch-based crack growth criterion, the delay of the initiation of crack growth in heterogeneous soft composites is predicted and compared to experimental observations. This work explains apparent toughening through the increase in critical applied stretch for crack growth through a bi-material interface: Qualitatively, an increase in the elastic contrast decreases the stress singularity, leading to lower stress ahead of the crack tip (Fig. 7b). Quantitatively, knowing critical values for a given material, one could predict the critical applied stretch for a crack to propagate through the bi-material interface.

CRediT authorship contribution statement

Chengyang Mo: Conceptualization, Methodology, Investigation, Writing – original draft. **Jordan R. Raney:** Conceptualization, Methodology, Writing – review & editing. **John L. Bassani:** Conceptualization, Methodology, Writing – review & editing.

Declaration of competing interest

The authors declare that they have no known competing financial interests or personal relationships that could have appeared to influence the work reported in this paper.

Acknowledgment

Appendix A. Solution procedure

The asymptotic boundary value problem $\nabla y_\alpha^{(i)} = 0$ is separable and the first two terms of the general solution is:

$$y_\alpha^{(i)} = r^m[p_\alpha^{(i)} \sin m\theta + q_\alpha^{(i)} \cos m\theta] \tag{A.1}$$

By plugging in (A.1) into the boundary conditions described in (11)–(13), six equations are derived with seven unknowns being $p_\alpha^{(1)}, p_\alpha^{(2)}, p_\alpha^{(3)}, q_\alpha^{(1)}, q_\alpha^{(2)}, q_\alpha^{(3)}$ and m:

$$p_\alpha^{(1)} \cos m\pi - q_\alpha^{(1)} \sin m\pi = 0 \tag{A.2}$$

$$p_\alpha^{(3)} \cos m\pi + q_\alpha^{(3)} \sin m\pi = 0 \tag{A.3}$$

$$p_\alpha^{(1)} \sin m\phi + q_\alpha^{(1)} \cos m\phi = p_\alpha^{(2)} \sin m\phi + q_\alpha^{(2)} \cos m\phi \tag{A.4}$$

$$p_\alpha^{(3)} \sin m(\phi - \pi) + q_\alpha^{(3)} \cos m(\phi - \pi) = p_\alpha^{(2)} \sin m(\phi - \pi) + q_\alpha^{(2)} \cos m(\phi - \pi) \tag{A.5}$$

$$p_\alpha^{(1)} \cos m\phi - q_\alpha^{(1)} \sin m\phi = s[p_\alpha^{(2)} \cos m\phi - q_\alpha^{(2)} \sin m\phi] \tag{A.6}$$

$$p_\alpha^{(3)} \cos m(\phi - \pi) - q_\alpha^{(3)} \sin m(\phi - \pi) = s[p_\alpha^{(2)} \cos m(\phi - \pi) - q_\alpha^{(2)} \sin m(\phi - \pi)] \tag{A.7}$$

After substitution and simplification, the following characteristic equation is derived:

$$\sin m\pi \left[\cos m\pi + \alpha \cos m(2\phi - \pi) \right] = 0 \tag{A.8}$$

This Eq. (A.8) divides the solution into two cases:

- **Case 1**: $\sin m\pi = 0$
  In this case, taking the lowest order solution yields $m = 1$:

$$y_\alpha^{(i)} = r[p_\alpha^{(i)} \sin \theta + q_\alpha^{(i)} \cos \theta] \tag{A.9}$$

  By plugging in (A.9) into (A.2) to (A.7), the solution can be obtained with one unknown parameter:

$$\begin{aligned} p_\alpha^{(1)} &= p_\alpha^{(3)} = 0, \\ p_\alpha^{(2)} &= \frac{(s-1)\sin\phi\cos\phi}{s\cos^2\phi + \sin^2\phi} q_\alpha^{(2)}, \\ q_\alpha^{(1)} &= q_\alpha^{(3)} = \frac{s}{s\cos^2\phi + \sin^2\phi} q_\alpha^{(2)} \end{aligned} \tag{A.10}$$

  Using these relations, one displacement solution that satisfies the governing equation and boundary condition is:

$$y_\alpha = \begin{cases} q_\alpha^{(2)} r \frac{s}{s\cos^2\phi + \sin^2\phi} \cos\theta, & \phi \le \theta \le \pi \\ q_\alpha^{(2)} r \left[\frac{(s-1)\sin\phi\cos\phi}{s\cos^2\phi + \sin^2\phi} \sin\theta + \cos\theta \right], & \phi - \pi \le \theta \le \phi \\ q_\alpha^{(2)} r \frac{s}{s\cos^2\phi + \sin^2\phi} \cos\theta, & -\pi \le \theta \le \phi - \pi \end{cases} \tag{A.11}$$

  Finally $q_\alpha^{(2)}$ is renamed to q_α since it is the amplitude for all regions:

$$y_\alpha = q_\alpha r h(\theta) \tag{A.12}$$

- **Case 2**: $\cos m\pi + \alpha \cos m(2\phi - \pi) = 0$
  After plugging in this relation back to (A.2) to (A.7), it is found $q_\alpha^{(2)} = 0$. Following that, the relations between other unknowns are:

$$\begin{aligned} p_\alpha^{(1)} &= -\frac{s\sin m\pi \cos m\phi}{\sin m(\phi - \pi)} p_\alpha^{(2)} \\ p_\alpha^{(3)} &= \frac{s\sin m\pi \cos m(\phi - \pi)}{\sin m\phi} p_\alpha^{(2)} \\ q_\alpha^{(1)} &= -\frac{s\cos m\pi \cos m\phi}{\sin m(\phi - \pi)} p_\alpha^{(2)} \\ q_\alpha^{(3)} &= -\frac{s\cos m\pi \cos m(\phi - \pi)}{\sin m\phi} p_\alpha^{(2)} \end{aligned} \tag{A.13}$$

  Using these relations (A.13), another displacement solution that satisfies the governing equation and boundary condition is:

$$y_\alpha = \begin{cases} p_\alpha^{(2)} r^m \frac{-s\cos m\phi}{\sin m(\phi - \pi)} \cos m(\theta - \pi), & \phi \le \theta \le \pi \\ p_\alpha^{(2)} r^m \sin m\theta, & \phi - \pi \le \theta \le \phi \\ p_\alpha^{(2)} r^m \frac{-s\cos m(\phi - \pi)}{\sin m\phi} \cos m(\theta + \pi), & -\pi \le \theta \le \phi - \pi \end{cases} \tag{A.14}$$

  Again $p_\alpha^{(2)}$ is renamed to just p_α which represents all regions:

$$y_\alpha = p_\alpha r^m g(\theta) \tag{A.15}$$

where m is the root of $\cos m\pi + \alpha \cos m(2\phi - \pi) = 0$.

Since the governing equation is linear, the two solutions found can be combined:

$$y_\alpha = p_\alpha r^m g(\theta) + q_\alpha r h(\theta) \tag{A.16}$$

Appendix B. Derivation of deformation gradient and left Cauchy–Green tensor

The deformation gradient $\mathbf{F} = \nabla \mathbf{y}$ is derived in the polar coordinates:

$$F_{ij} = \frac{\partial y_i}{\partial x_j} = \frac{\partial y_i}{\partial r}\frac{\partial r}{\partial x_j} + \frac{\partial y_i}{\partial \theta}\frac{\partial \theta}{\partial x_j} \tag{B.1}$$

where the Jacobian of transformation from cartesian (x_1, x_2) to polar coordinates (r, θ) is:

$$\mathbf{J}(r,\theta) = \begin{bmatrix} \frac{\partial r}{\partial x_1} & \frac{\partial r}{\partial x_2} \\ \frac{\partial \theta}{\partial x_1} & \frac{\partial \theta}{\partial x_2} \end{bmatrix} = \begin{bmatrix} \cos\theta & \sin\theta \\ -\frac{\sin\theta}{r} & \frac{\cos\theta}{r} \end{bmatrix} \tag{B.2}$$

Plugging the Jacobian (B.2) and solution (14) into (B.1) to obtain:

$$\begin{aligned}
F_{11} &= p_1 r^{m-1} m g(\theta)\cos\theta - p_1 r^m g'(\theta)\sin\theta/r + q_1 h(\theta)\cos\theta - q_1 r h'(\theta)\sin\theta/r \\
&= p_1 r^{m-1}[mg(\theta)\cos\theta - g'(\theta)\sin\theta] + q_1[h(\theta)\cos\theta - h'(\theta)\sin\theta] \\
F_{12} &= p_1 r^{m-1} m g(\theta)\sin\theta + p_1 r^m g'(\theta)\cos\theta/r + q_1 h(\theta)\sin\theta + q_1 r h'(\theta)\cos\theta/r \\
&= p_1 r^{m-1}[mg(\theta)\sin\theta + g'(\theta)\cos\theta] + q_1[h(\theta)\sin\theta + h'(\theta)\cos\theta] \\
F_{21} &= p_2 r^{m-1} m g(\theta)\cos\theta - p_2 r^m g'(\theta)\sin\theta/r = p_2 r^{m-1}[mg(\theta)\cos\theta - g'(\theta)\sin\theta] \\
F_{22} &= p_2 r^{m-1} m g(\theta)\sin\theta + p_2 r^m g'(\theta)\cos\theta/r = p_2 r^{m-1}[mg(\theta)\sin\theta + g'(\theta)\cos\theta]
\end{aligned} \tag{B.3}$$

The Cauchy stress are computed from the left Cauchy–Green tensor $\mathbf{B} = \mathbf{FF}^T$. Each component of $\mathbf{B}$ as following:

$$\begin{aligned}
B_{11} &= F_{11}^2 + F_{12}^2 = p_1^2 r^{2m-2}\left[\left[mg(\theta)\cos\theta - g'(\theta)\sin\theta\right]^2 + \left[mg(\theta)\sin\theta + g'(\theta)\cos\theta\right]^2\right] \\
&\quad + q_1^2\left[\left[h(\theta)\cos\theta - h'(\theta)\sin\theta\right]^2 + \left[h(\theta)\sin\theta + h'(\theta)\cos\theta\right]^2\right] \\
&\quad + 2p_1 q_1 r^{m-1}\left[mg(\theta)h(\theta)\cos^2\theta + g'(\theta)h'(\theta)\sin^2\theta - mg(\theta)h'(\theta)\cos\theta\sin\theta - g'(\theta)h(\theta)\cos\theta\sin\theta\right] \\
&\quad + 2p_1 q_1 r^{m-1}\left[mg(\theta)h(\theta)\sin^2\theta + g'(\theta)h'(\theta)\cos^2\theta + mg(\theta)h'(\theta)\cos\theta\sin\theta + g'(\theta)h(\theta)\cos\theta\sin\theta\right] \\
&= p_1^2 r^{2m-2}\left[m^2 g^2(\theta) + g'^2(\theta)\right] + 2p_1 q_1 r^{m-1}\left[mg(\theta)h(\theta) + g'(\theta)h'(\theta)\right] + q_1^2\left[h^2(\theta) + h'^2(\theta)\right] \\
B_{12} &= F_{11}F_{12} + F_{21}F_{22} = p_1 p_2 r^{2m-2}\left[\left[mg(\theta)\cos\theta - g'(\theta)\sin\theta\right]^2 + \left[mg(\theta)\sin\theta + g'(\theta)\cos\theta\right]^2\right] \\
&\quad + p_2 q_1 r^{m-1}\left[mg(\theta)h(\theta)\cos^2\theta + g'(\theta)h'(\theta)\sin^2\theta - mg(\theta)h'(\theta)\cos\theta\sin\theta - g'(\theta)h(\theta)\cos\theta\sin\theta\right] \\
&\quad + p_2 q_1 r^{m-1}\left[mg(\theta)h(\theta)\sin^2\theta + g'(\theta)h'(\theta)\cos^2\theta + mg(\theta)h'(\theta)\cos\theta\sin\theta + g'(\theta)h(\theta)\cos\theta\sin\theta\right] \\
&= p_1 p_2 r^{2m-2}\left[m^2 g^2(\theta) + g'^2(\theta)\right] + p_2 q_1 r^{m-1}\left[mg(\theta)h(\theta) + g'(\theta)h'(\theta)\right]
\end{aligned}$$

$$\tag{B.4}$$
$$\tag{B.5}$$

$$\begin{aligned}
B_{22} &= F_{21}^2 + F_{22}^2 = p_2^2 r^{2m-2}\left[\left[mg(\theta)\cos\theta - g'(\theta)\sin\theta\right]^2 + \left[mg(\theta)\sin\theta + g'(\theta)\cos\theta\right]^2\right] \\
&= p_2^2 r^{2m-2}\left[m^2 g^2(\theta) + g'^2(\theta)\right]
\end{aligned} \tag{B.6}$$

Define $G(\theta) = m^2 g^2(\theta) + g'^2(\theta)$, $H(\theta) = h^2(\theta) + h'^2(\theta)$ and $GH(\theta) = mg(\theta)h(\theta) + g'(\theta)h'(\theta)$. The matrix form of $\mathbf{B}$ can be expressed as:

$$\mathbf{B} = r^{2m-2}G(\theta)\begin{bmatrix} p_1^2 & p_1 p_2 \\ p_1 p_2 & p_2^2 \end{bmatrix} + r^{m-1}GH(\theta)\begin{bmatrix} 2p_1 q_1 & p_2 q_1 \\ p_2 q_1 & 0 \end{bmatrix} + H(\theta)\begin{bmatrix} q_1^2 & 0 \\ 0 & 0 \end{bmatrix} \tag{B.7}$$

Appendix C. Supplementary data

Supplementary video related to this article can be found online at https://doi.org/10.1016/j.jmps.2021.104653.

References

Bassani, J.L., Erdogan, F., 1979. Stress intensity factors in bonded half planes containing inclined cracks and subjected to antiplane shear loading. Int. J. Fract. 15 (2), 145–158.

Bogy, D.B., 1971. On the plane elastostatic problem of a loaded crack terminating at a material interface. Acta Mech. Solida Sin. 38 (4), 911–918.

Cai, Li-Heng, Kodger, Thomas E., Guerra, Rodrigo E., Pegoraro, Adrian F., Rubinstein, Michael, Weitz, David A., 2015. Soft poly(dimethylsiloxane) elastomers from architecture-driven entanglement free design. Adv. Mater. 27 (35), 5132–5140.

Chang, Jun, Xu, Jin Quan, 2007. The singular stress field and stress intensity factors of a crack terminating at a bimaterial interface. Int. J. Mech. Sci. 49 (7), 888–897.

Cook, T.S., Erdogan, F., 1972. Stresses in bonded materials with a crack perpendicular to the interface. Internat. J. Engrg. Sci. 10 (8), 677–697.

Cox, Lewis M., Blevins, Adrienne K., Drisko, Jasper A., Qi, Yuan, Ding, Yifu, Fiedler-Higgins, Callie I., Long, Rong, Bowman, Christopher N., Killgore, Jason P., 2019. Tunable mechanical anisotropy, crack guiding, and toughness enhancement in two-stage reactive polymer networks. Adv. Energy Mater. 21 (8), 1900578.

Geubelle, Philippe H., Knauss, Wolfgang G., 1994a. Finite strains at the tip of a crack in a sheet of hyperelastic material: I. Homogeneous case. J. Elasticity 35 (1–3), 61–98.

Geubelle, Philippe H., Knauss, Wolfgang G., 1994b. Finite strains at the tip of a crack in a sheet of hyperelastic material: II. Special bimaterial cases. J. Elasticity 35 (1–3), 99–137.

Geubelle, Philippe H., Knauss, Wolfgang G., 1994c. Finite strains at the tip of a crack in a sheet of hyperelastic material: III. General bimaterial case. J. Elasticity 35 (1–3), 139–174.

Hamdi, A., Aït Hocine, Nourredine, Abdelaziz, M. Naït, Benseddiq, N., 2007. Fracture of elastomers under static mixed mode: The strain-energy-density factor. Int. J. Fract. 144 (2), 65–75.

He, Ming-Yuan, Hutchinson, John W., 1989. Crack deflection at an interface between dissimilar elastic materials. Int. J. Solids Struct. 25 (9), 1053–1067.

Kim, Tae Kyung, Kim, Jeong Koo, Jeong, Ok Chan, 2011. Measurement of nonlinear mechanical properties of PDMS elastomer. Microelectron. Eng. 88 (8), 1982–1985, Proceedings of the 36th International Conference on Micro- and Nano-Engineering (MNE).

Knowles, J.K., Sternberg, Eli, 1973. An asymptotic finite-deformation analysis of the elastostatic field near the tip of a crack. J. Elasticity 3 (2), 67–107.

Knowles, J.K., Sternberg, Eli, 1974. Finite-deformation analysis of the elastostatic field near the tip of a crack: Reconsideration and higher-order results. J. Elasticity 4 (3), 201–233.

Knowles, J.K., Sternberg, Eli, 1983. Large deformations near a tip of an interface-crack between two Neo-Hookean sheets. J. Elasticity 13 (3), 257–293.

Liu, Yin, Moran, Brian, 2020a. Asymptotic path-independent integrals for the evaluation of crack-tip parameters in a neo-Hookean material. Int. J. Fract. 224 (1), 133–150.

Liu, Yin, Moran, Brian, 2020b. Large deformation near a crack tip in a fiber-reinforced neo-Hookean sheet. J. Mech. Phys. Solids 143, 1–29.

Long, Rong, Hui, Chung Yuen, 2015. Crack tip fields in soft elastic solids subjected to large quasi-static deformation - a review. Extrem. Mech. Lett. 4, 131–155.

Lu, Yinan, Qi, Yuan, Tenardi, Michely, Long, Rong, 2021. Mixed-mode fracture in a soft elastomer. Extrem. Mech. Lett. 101380.

Rivlin, R.S., Thomas, A.G., 1953. Rupture of rubber. I. Characteristic energy for tearing. J. Polym. Sci. 10 (3), 291–318.

Ru, Chong Qing, 1997. Finite strain singular field near the tip of a crack terminating at a material interface. Math. Mech. Solids 2 (1), 49–73.

Shan, Sicong, Kang, Sung H., Raney, Jordan R., Wang, Pai, Fang, Lichen, Candido, Francisco, Lewis, Jennifer A., Bertoldi, Katia, 2015. Multistable architected materials for trapping elastic strain energy. Adv. Mater. 27 (29), 4296–4301.

Thomas, A.G., 1958. Rupture of rubber. V. Cut growth in natural rubber vulcanizates. J. Polym. Sci. 31 (123), 467–480.

Wang, Zhengjin, Xiang, Chunping, Yao, Xi, Le Floch, Paul, Mendez, Julien, Suo, Zhigang, 2019. Stretchable materials of high toughness and low hysteresis. Proc. Natl. Acad. Sci. 201821420.

Wong, Felix S., Shield, Richard T., 1969. Large plane deformations of thin elastic sheets of neo-Hookean material. Z. Angew. Math. Phys. ZAMP 20 (2), 176–199.

Zak, A.R., Williams, M.L., 1963. Crack point stress singularities at a bi-material interface. J. Appl. Mech. 30 (1), 142–143.